Photocatalytic Nitrogen Reduction by Ti_3C_2 MXene Derived Oxygen Vacancy-rich C/TiO_2

Jing Qian[a], Sen Zhao[a], Wenqiang Dang[c], Yuan Liao[a], Wen Zhang[a], Hui Wang[b], Lingling Lv[d], Lei Luo[a], Hai-Ying Jiang*[a], Junwang Tang*[b]

[a] Key Lab of Synthetic and Natural Functional Molecule Chemistry of Ministry of Education, and the Energy and Catalysis Hub, College of Chemistry and Materials Science, Northwest University, Xi'an 710127, People's Republic of China

[b] Department of Chemical Engineering, University College London, Torrington Place, London WC1E 7JE, U.K.

[c] Department of Physics, Tianshui Normal University, Tianshui, Gansu, 741001, People's Republic of China.

[d] College of Chemical Engineering and Technology, Tianshui Normal University, Tianshui, Gansu, 741001, People's Republic of China.

Jing Qian and Sen Zhao contribute experiments equally to this paper; Wenqiang Dang contribute the main DFT calculations.

jianghy@nwu.edu.cn, junwang.tang@ucl.ac.uk

Abstract

In this work, oxygen vacancy-rich C/TiO_2 (OV-C/TiO_2) samples were prepared by a one-step calcination approach using Ti_3C_2 MXene as the precursor, and used for the photocatalytic N_2 reduction. The NH_3 yields of all the prepared OV-C/TiO_2 samples exceeded those achieved on commercial anatase TiO_2 and P25, with both H_2O and CH_3OH as the proton sources. Among them, the OV-C/TiO_2-600 offered the remarkable NH_3 synthesis rates, which are 41.00 μmol g^{-1} h^{-1} (with H_2O as the proton source) and 84.00 μmol g^{-1} h^{-1} (with CH_3OH as the proton sources). The photocurrent and fluorescence spectra showed that OV-C/TiO_2-600 exhibited the highest generation/separation rate and longest lifetime of photocarriers among all the prepared samples. ESR and TPD experiments confirmed much more efficient chemisoption of N_2 on the surface of the prepared OV-C/TiO_2-600 than that on the surface of the commercial anatase TiO_2. Moreover, DFT calculations further demonstrated that N_2 conversion to NH_3 through a Gibbs free energy release leading alternating pathway with a low energy barriers, on the oxygen vacancy on TiO_2 surface.

1. Introduction

Reduction of N_2 to NH_3 is a vital process to promote the growth of the organism.[1-4] In nature, biological nitrogen fixation and light-driven nitrogen fixation are two main pathways for NH_3 synthesis. However, productions of NH_3 by the two approaches are far away from the agricultural requirements. Hence, artificial nitrogen fixation is a pressing demand for solving the global starvation problem.[5] More than a century ago, German chemist Fritz Haber contrived Haber-Bosch process to manufacture NH_3 by N_2 and H_2 at drastically high temperature (> 673 K) and pressure (> 200 bar).[6-10] About a decade ago, Greek chemists Marnellos and Stoukides synthesized NH_3 using H_2 and N_2 diluted by He in an electrolytic cell with the solid electrolyte of strontium-cerium-yttrium-perovskite porous ceramics at 843 K and atmospheric pressure, improving NH_3 yield from 15% (Haber-Bosch process) to 78%.[11] Notably, the reaction conditions of the two methods are still very harsh with intensive energy consumption and environmental pollution.[12] Thus a safe, clean and sustainable NH_3 synthesis processes are urgently demanded.[13]

Semiconductor photocatalysis as a clean and sustainable technology has been applied in many fields, such as water splitting, pollutant elimination, CO_2 reduction, CH_4 activation, as well as N_2 fixation.[14] As early as in 1977, Schrauzer and Guth reported the groundbreaking research on photolysis of N_2 to NH_3 on TiO_2.[15] Since then, the photocatalytic N_2 fixation becomes highly attractive as a promising strategy for NH_3 synthesis under mild conditions.[16-22] However, its development is barely satisfactory for the long term in the following decades.[23] This is due to the difficulty of breaking the highly stable N≡N triple bond, whose bond energy is as high as 941 kJ/mol.[4] This is still an enormous challenge for all scientists today. Until recently, some prospective semiconductors, TiO_2,[4, 12, 15, 24-32] $SrTiO_3$,[33] $BaTiO_3$,[34] CdS,[6] BiOX,[1, 23, 35-37] g-C_3N_4,[38-41] and WO_3,[42, 43] have been successively used for photocatalytic N_2 fixation. Among them, TiO_2-based semiconductors are the most stable and robust photocatalysts, but they still suffer from low efficiency. Notably, oxygen vacancies on the surface of TiO_2[4, 12] and BiOBr[1, 23] have been proved to be effective for photocatalytic N_2 fixation, due to their favorable adsorption of N_2 molecules and high reduction potential of conduction band electrons. Hence, constructing oxygen vacancies on the surface of semiconductors is a promising strategy to improve the photocatalytic efficiency of N_2 fixation.

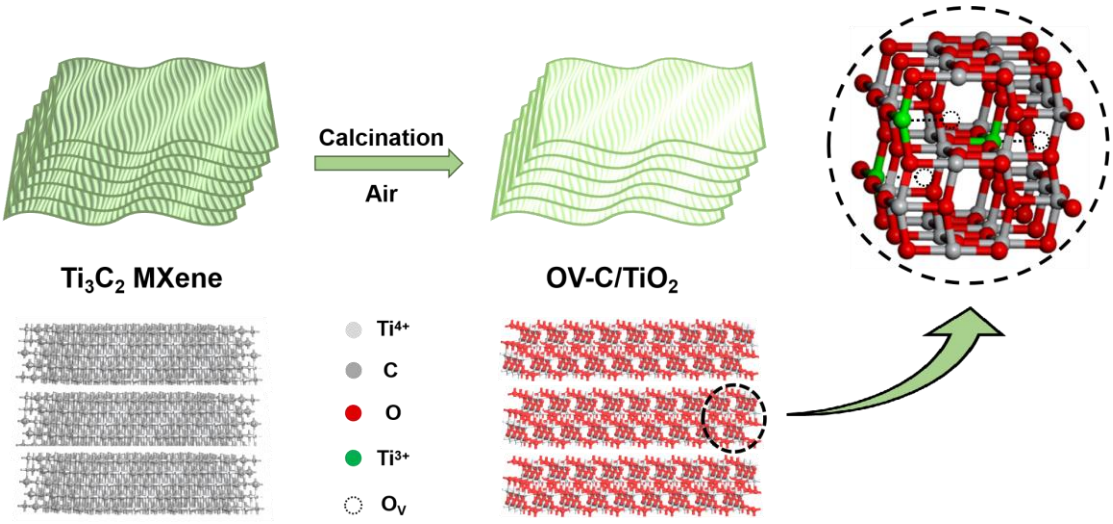

Scheme 1 Diagram of the preparation process of OV-C/TiO_2.

Ti_3C_2 MXene is a new layered material without noble metal, which was firstly synthesized in 2011[44] and has been widely applied as co-catalysts in photocatalysis [45-51]. Meanwhile, it is also a good TiO_2 precursor, from which abundance of vacancies can be created.[52, 53] Herein, OV-C/TiO_2 samples were prepared through one calcination step by using Ti_3C_2 MXene as the precursor (Scheme 1), which was synthesized by etching Al layers from the Ti_3AlC_2 in HF at room temperature [54]. Abundance of oxygen vacancies and C doping was observed in the as-prepared TiO_2 sample. Hence, this OV-C/TiO_2 was prospected to have a high ability to convert N_2 to NH_3 under sunlight irradiation. The experimental results in this work showed that, over all the prepared OV-C/TiO_2 samples under full spectrum light irradiation, NH_3 was successfully generated from N_2 with either H_2O and CH_3OH as the proton source. Remarkably, the efficiency of N_2 fixation was achieved at the OV-C/TiO_2-600 sample. All the data of NH_3 yields were detected by ion chromatography method to prove the effectiveness of the photocatalyst.[55] The origin of the N source of the produced NH_3 was studied by the isotope labeled N_2 ($^{14}N_2$ and $^{15}N_2$), the different products were identified by ^1H spectra of nuclear magnetic resonance (NMR). This excellent N_2 fixation was proposed due to high generation/separation rate of photocarriers with prolonged lifetime, the efficient N_2 adsorption on the abundance of oxygen vacancies, as well as the low-energy-barrier pathway of N_2 to NH_3 on oxygen vacancy. The mechanism of high photocatalytic activity for NH_3 synthesis over OV-C/TiO_2 we prepared were further discussed based on the measurements of photoelectrochemical experiments, fluorescence spectra, electron

spin-resonance spectroscopy (ESR), temperature programmed desorption (TPD) and DFT calculations.

2. Experimental Section

2.1. Materials

Ti_3AlC_2 MAX phase powders (>98 wt% purity) were purchased from Laizhou Kaixi Ceramic Materials Co., Ltd. (Shandong, China). Ethanol (AR) and hydrofluoric acid were purchased from Sinopharm Chemical Reagent Co., Ltd. Ammonium chloride and sodium hydroxide and sodium were obtained from Shanghai Aladdin Bio-Chem Technology Co., Ltd. Ultrapure water (18.2 MΩ cm) used throughout all experiment was purified through Millipore Milli-Q system. All chemical reagents were used as received without further purification.

2.2. Preparation of OV-C/TiO_2

Ti_3C_2 MXene was synthesized by HF-etching method according to the reported literature.[54] In detail, 1 g of Ti_3AlC_2 was added into 20 mL 40% HF solution with magnetic stirring at room temperature for 24 hours. The resulting product was washed with deionized water and ethanol several times until pH > 6. The precipitates were sonicated with the dispersion of water for 1 hour and then centrifuged at 3500 rpm for 1 hour to obtain Ti_3C_2 MXene. To prepare OV-C/TiO_2, the prepared Ti_3C_2 MXene was heated to different temperatures (400, 500, 600, 700 and 800℃, respectively) in air at a rate of 5℃/min and kept for 2 hours. The resultant samples were denoted as OV-C/TiO_2-X, herein X represents the annealing temperature, being 400, 500, 600, 700 and 800, respectively.

2.3. Characterizations

The SEM images were collected from Hitachi SU-8010 scanning electron microscopy with an operating voltage of 5 kV. The TEM and HRTEM images were performed using an FEI Tecnai G2 F20 transmission electron microscope operated at 200 kV. The specific surface areas were determined using a surface analyzer (Tristar II3020) through nitrogen adsorption and desorption isotherms at 77 K by Brunauer-Emmett-Teller (BET) method. The XRD patterns were recorded on a Bruker AXS-D8 diffractometer using Cu Kα radiation. The UV-vis DRS spectra were recorded

by UV-vis spectrophotometer (U-3310, HITACHI) equipped with a diffuse reflectance accessory, using $BaSO_4$ as the reflectance standard reference. The low temperature ESR spectra were recorded on a Bruker EXM EPR Spectrometer at 77 K. The XPS experiments were carried out by PHI 5000 VersaProbe II XPS system. All binding energies were referenced with respect to the C1s peak (284.6 eV) of the surface adventitious carbon. The photoluminescence spectra decay curves were obtained by using FLsp920 with EPL375 as the light source. The adsorptions of N_2 on the surface of the commercial TiO_2 and prepared OV-C/TiO_2-600 were performed on a TPD equipment (Maike, Autochem II 2920, TCD detector). Specifically, 100 mg sample was pretreated at 300 ℃ for 2 hours, and then heated to 450 ℃ at a rate of 10 ℃/min with a gas flow rate of 50 mL/min, and kept for two hours.

2.4. Electrochemical tests

The Transient photocurrent responses was performed on a Princeton 283 electrochemical workstation equipped with a standard three-electrode cell with 1M Na_2SO_4 as the electrolyte and a Xe-lamp (HSX-F/UV 300) as the light source. An ITO glass electrode (20×30×0.4mm, 7-10 Ω) coated with photocatalyst (drop coating), a platinum foil and a saturated calomel electrode were employed as the working electrode, the counter electrode and the reference electrode respectively.

EIS test was performed on CHI 660E electrochemistry workstation (Chenhua Instrument) with a standard three-electrode cell system. The working electrode was a glassy carbon electrode (d = 3 mm, S = 0.0707 cm^2), the counter electrode was a platinum foil and the reference electrode was a saturated calomel electrode. For preparing working electrode, 5 mg of powder and 0.1 mL of Nafion solution (5 wt %) were dispersed in 0.9 mL absolute ethanol to form a homogeneous ink, and 4 μL ink was loaded onto glassy carbon electrode via drop coating technique. Electrochemical impedance spectra (EIS) were conducted in the frequency range of 1 mHz to 100 kHz under relatively open circuit voltage, using 0.5 M $NaSO_4$ solution as electrolyte. The EIS spectra were collected both under light irradiation and in the dark.

2.5. Photocatalytic nitrogen reduction

The photocatalytic N_2 reduction experiments were carried out in N_2 atmosphere at room temperature using a 300 W Xe lamp (PLS-SXE300D, 200-800 nm) as the light source, with either

H_2O or CH_3OH as the proton source. Typically, 50 mg of catalyst was dispersed in 50 mL of ultrapure water and then transferred to the reactor equipped with water circulation in the outer jacket in order to maintain at the temperature of 25 ℃. The methanol concentrations in the system are 0.01 M, when using methanol as the proton source. Before irradiation, the mixture was continuously stirred in the dark with pure N_2 (99.999%) bubbling at a flow rate of 50 ml min^{-1} for 30 minutes and then irradiated for 120 minutes. During the period of a photocatalytic reaction, 1 mL of the solution was sampled every 30 minutes for product analysis. The ammonia concentration was detected by ion chromatography (IC, SHINE CIC-D120) equipped with an Ionpac CS16 column (4 × 250 mm, Dionex), a suppressor (SHY-A/C), and a conductivity detector. The eluent was 30 mM CH_4O_3S solution, the flow rate was 0.5 mL/min, and the suppress current was 50 mA. Notably, ion chromatography (IC) method is much more reliable than Nessler or indophenol blue (IB) method.[55] Before catalysts were removed by filtration, 500 μL 0.1 M HCl solution was added to 500 μL suspension for 5 minutes. Consequently, the obtained solutions were diluted by 4 mL ultrapure water for measurement. The retention time of NH_4^+ is at about the 11th minute. Absolute calibration of the method was done using ammonium chloride solutions of known concentration as standards.

The photocatalytic generations of ·OH over OV-C/TiO_2-600 sample was measured by a fluorescence method using coumarin as a chemical trap.[56] The photocatalysts were dispersed in a 30ml aqueous solution of 1 mM coumarin, and stirred for 30 min in the dark before UV-vis light irradiation. 3 ml suspension was sampled and separated by centrifugation at a given irradiation time interval (5 min). The fluorescence emission intensity evolution of 7-hydroxycomumarin (7-HC), a highly fluorescent product formed by the coumarin and ·OH, was detected at about 450 nm under the excitation at 350 nm using a spectrofluorometer (PerkinElmer LS55).

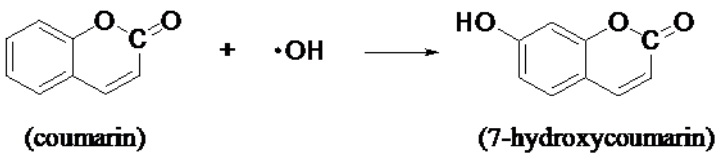

(coumarin) (7-hydroxycoumarin)

The production of the liquid product HCHO was measured by colorimetry.[57] Specifically, 15 g of ammonium acetate, 0.3 mL of acetic acid, and 0.2 mL of pentane-2,4-dione were dissolved in

water to prepare 100 ml of a color reagent aqueous solution. After diluting 0.5 mL of the test solution with 2 mL of water, mixed it with 0.5 mL of the chromogenic reagent aqueous solution and maintained at room temperature for 1 hour. The absorbance at 412 nm was measured by UV-Vis absorption spectroscopy.

The apparent quantum yields (AQY) were determined using monochromatic filter of 400 nm and 420 nm with a bandwith of 5 nm, to carried out the photocatalytic N_2 reduction. The calculated as follows:[12]

AQY = 100% × (3 × generated ammonia molecular number) / incident photon number

2.6. $^{15}N_2$ isotope Labeling Experiments [58]

An isotope labeling experiments were carried out to clarify the N source of generated NH_3, by using $^{14}N_2$ and $^{15}N_2$ as the feeding gas. The $^{14}NH_3$ and $^{15}NH_3$ were distinguished by NMR spectra of ^1H of NH_4^+. As displayed in Figure S1, the NMR peak of ^1H is divided into triple peaks by ^{14}N and and double peaks by ^{15}N isotopes, for standard $^{14}NH_4Cl$ and $^{15}NH_4Cl$. The number of peaks (*N*) in accordance with the theory calculations: $N = 2nI + 1$. This formula means that the NMR peak of ^1H will be divided to several peaks due to N isotopes, where *n* represents the number of N atoms, and *I* is the spin quantum number of isotope N: $I = 1$ for ^{14}N and $I = 1/2$ for ^{15}N. In addition, from Figure S1, the coupling constant of the triple peaks is 52.3 Hz for $^{14}NH_4Cl$, while the coupling constant of double peaks is 73.2 Hz for $^{15}NH_4Cl$.

After the photocatalytic NH_3 synthesis by OV-C/TiO_2-600 for 2 hours, the obtained $^{14}NH_3$ and $^{15}NH_3$ were distinguished by ^1H nuclear magnetic resonance (NMR, 400 MHz). The typical NMR signals of ^1H for $^{14}NH_4^+$ and $^{15}NH_4^+$ were detected using $^{14}N_2$ and $^{15}N_2$ as the feeding gas. In this process, the prepared NH_3 solutions were concentrated by distillation before being added to deuterated DMSO.

2.7. DFT calculations

The spin-polarized projector augmented wave (PAW) pseudopotentials via the Vienna Ab initio Simulation Program (VASP) were used to perform the density functional theory (DFT) calculations.[59-62] The exchange and correlation energy were described by the generalized gradient

approximation (GGA) via Perdew-Burke-Ernzerhof (PBE) functional.[63] The constituted atomic valence states adopted were H $1s^2$, N $2s^22p^3$, O $2s^22p^4$, and Ti $3p^63d^34s^1$. The plane wave cut-off energy was 450 eV and a 7×7×3 grid of Monkhorst-pack points were employed for geometry optimization of a 12-atom conventional cell of anatase TiO_2.[64] Geometry optimizations were obtained by minimizing the total energy using a quasi-Newton algorithm to relax ions until it converged within 10^{-4} eV and the forces on each ion were less than 0.05 eV/Å. During the geometry optimization, volume and shape of the cell as well as atomic positions were relaxed.[45]

For the anatase (1 0 1) surface with an oxygen vacancy (S_{OV}), a vacuum region of at least 15 Å was used, so that the slabs in neighbouring cells in the vertical direction are separated by a sufficiently large distance. During the geometry optimization, the first three O-Ti-O-layers of the atoms were allowed to relax until reaching a 10^{-4} eV convergence in the total energy, while the forces on each ion were less than 0.05 eV/Å with the three remaining O-Ti-O-layers being kept fixed (bulk like). To avoid the interaction among adsorbed molecules in neighboring cells, supercells with 10.3×15.2 Å units of surfaces are constructed.[45] To investigate the mechanisms of N_2 reduction on the oxygen vacancy on TiO_2 surface, we carried out the DFT-D3 method with Becke-Jonson damping.[65, 66] We studied the most plausible N_2 adsorption configuration on the S_{OV}. The structure after the geometric relaxation is shown in Figure S2, which was drawn using the VESTA software.[67]

The adsorption energy (E_{ads}) was calculated using the equation:

$$\Delta E = E_{ads} = E_{gas@Sov} - E_{Sov} - E_{gas} \qquad (1)$$

In Eq. 1, ΔE is the reaction energy, E_{Sov} is the total energy of the anatase (1 0 1) surface with an oxygen vacancy, $E_{gas@Sov}$ is the total energy of E_{Sov} with gas adsorbed, and E_{gas} is the total energy of the isolated species (N_2, NH_3, $H^+ + e^-$). In the present models, the chemical potential of a proton-electron pair, $\mu(H^+) + \mu(e^-)$, was equal to the half of the chemical potential of one gaseous hydrogen, $1/2\ \mu(H_2)$.

In all fundamental reaction steps, reaction Gibbs free energy changes were calculated using formula:[68-70]

$$\Delta G = \Delta E + \Delta ZPE - T\Delta S \qquad (2)$$

In Eq. 2, ΔZPE is the difference to zero point energies due to the reaction,[66] and ΔS is the entropy

change, respectively. Because the temperature T = 0 K was used in the ΔG calculation of each reaction step, Eq (1) can be written as:

$$\Delta G = \Delta E + \Delta ZPE \qquad (3),$$

meaning ΔG are corrected via computing the vibrational frequencies of surface species for the ΔZPE.

3. Results and Discussions

3.1. **Characterizations**

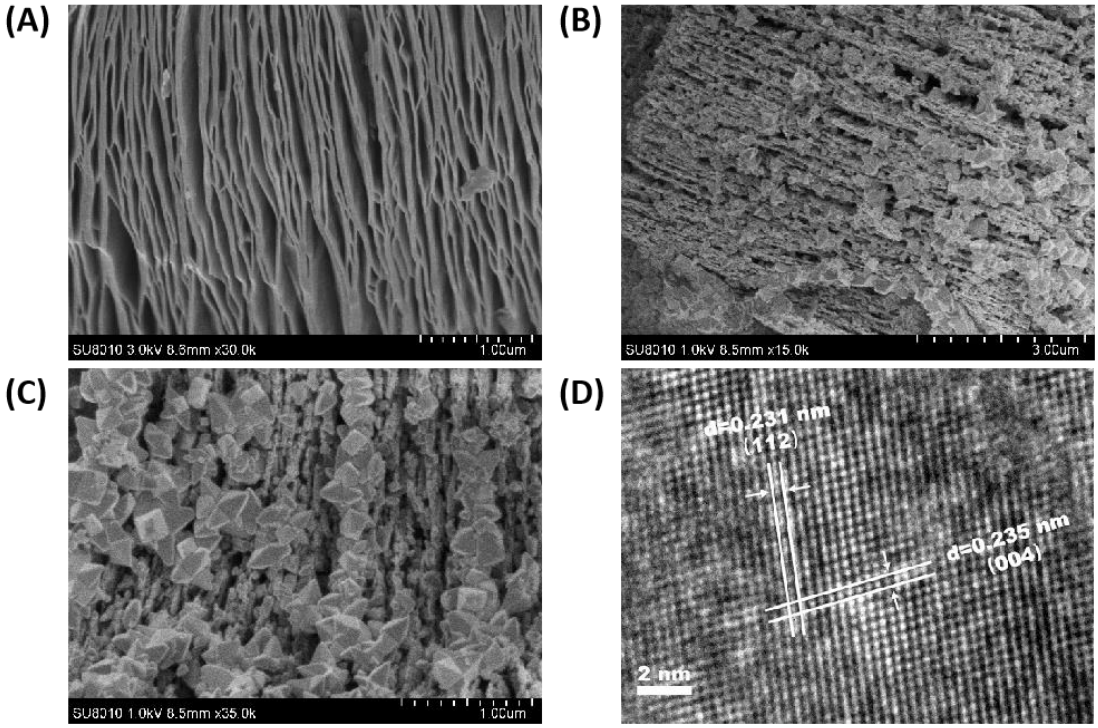

Figure 1 (A) SEM image of Ti_3C_2 MXene, (B) and (C) SEM images of OV-C/TiO_2-600, (D) HRTEM image of OV-C/TiO_2-600.

The micromorphology and architectural structures of Ti_3C_2 MXene and the calcined OV-C/TiO_2 samples were characterized by scanning electron microscopy (SEM). In Figure 1A, the layered structure of Ti_3C_2 MXene is clearly observed, which comes from etching the Al layers of Ti_3AlC_2 MAX phase.[52, 53] After the oxidation at high temperature in air, its layered structure remained (Figure 1B and S3-6). Meanwhile, type II adsorption isotherms in Figure S7 also suggest multilayer structures of Ti_3C_2 MXene and as-prepared samples.[71] The surface areas of all the prepared samples were also evaluated by Brunauer-Emmett-Teller method and listed in Table S1.

All samples show relatively small surface areas, while OV-C/TiO_2-600 has the largest of 16.9 m^2 g^{-1}. As shown in Figure 1C, large amounts of small crystal particles (100 nm - 300 nm) with regular octahedral structure were formed along with the layers. The crystal structure of the particles was further identified by high-resolution transmission electron microscopy (HRTEM) in Figure 1D. Two sets of intersectant fringes with the lattice spacing of 0.231 nm and 0.235 nm can be indexed to (112) and (004) planes of anatase TiO_2,[72] while no crystal lattice of Ti_3C_2 MXene was found.[52]

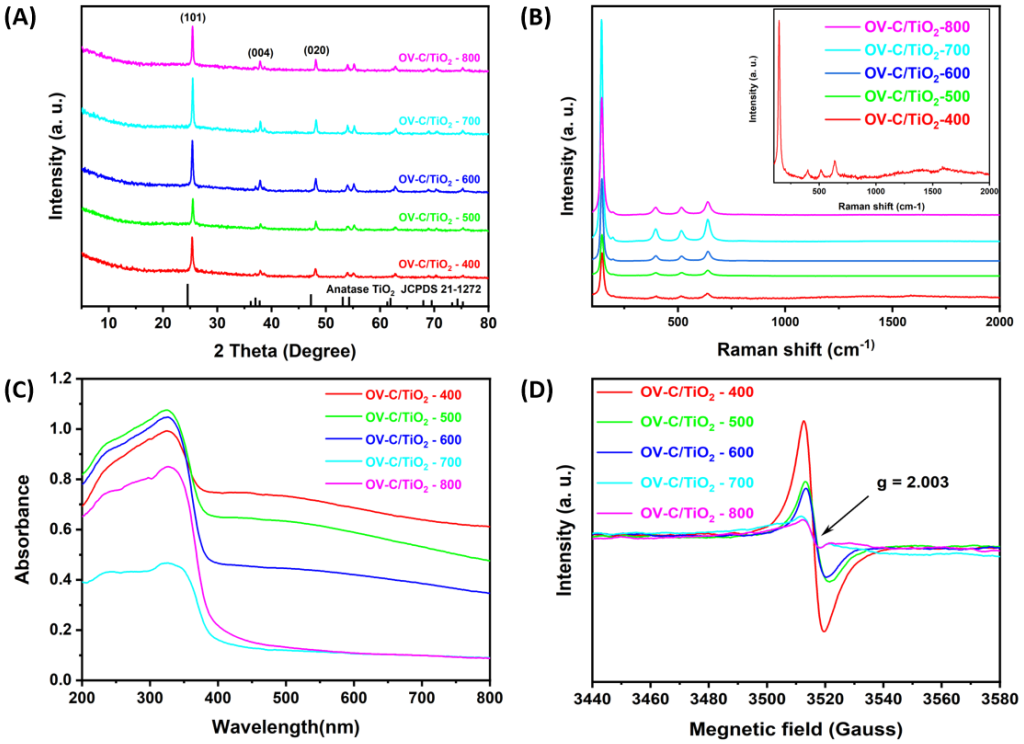

Figure 2 (A) XRD full spectra, (B) Raman spectra (inset: Ranman spectra of OV-C/TiO_2-400), (C) UV-vis DRS spectra, (D) ESR spectra of OV-C/TiO_2 derived by Ti_3C_2 MXenes calcined at different temperatures.

The crystal structures of calcined samples were further confirmed by X-ray diffractometer spectra. The XRD patterns described in Figure 2A show good tetragonal crystal phase of anatase TiO_2, all the peaks are in accordance with the standard database (JCPDS No. 21-1272) of anatase TiO_2, while no (002) peak of Ti_3C_2 MXene crystal appears at 9°-10°.[52] The crystal lattice parameters of OV-C/TiO_2-600 calculated by Jade 5 are listed in Table S2, which is consistent with the results of HRTEM in Figure 1D. Raman spectra (Figure 2B) was also obtained to confirm the

conversion of Ti_3C_2 MXene to TiO_2. The four sharp peaks below 750 cm^{-1} for all the samples are attributed to the band modes of TiO_2,[45, 52] while the wide peak at the range of 1000 - 2000 cm^{-1} for the sample of OV-C/TiO_2-400 (inset of Figure 2B) were attributed to the residual of Ti_3C_2 MXene.[45] However, the peaks derived from residual Ti_3C_2 MXene disappeared when the calcination temperature is higher than 500℃, suggesting the absolute conversion of Ti_3C_2 MXene to TiO_2. Meanwhile, no peaks at 1350 cm^{-1} and 1590 cm^{-1} related to amorphous carbon [52] are observed in the Raman spectra of all the samples prepared at the temperature higher than 400 ℃. More detailed observation in Figure S8 indicates that (101) diffraction peaks of the prepared OV-C/TiO_2 samples significantly shift to higher 2θ values compared with the standard data, but no regulation with the increase of the calcination temperature. According to Bragg's law, the high 2θ value of the diffraction peaks means shrinkage of the crystal lattice, while the low 2θ value means an expansion of the crystal lattice.[71] Therefore, C doping was proposed, which could cause the 2θ angle shifts to smaller value, but be offset by oxygen vacancies.[55] The unclear trend was thus believed due to the cooperative effects of the oxygen vacancies introduction and C doping. [12, 74]

The introduction of oxygen vacancies can also be proved by UV-vis diffuse reflectance (UV-vis DRS) and electron spin-resonance spectroscopy (ESR). As displayed in Figure 2C, all samples exhibit an extended absorption in the range of 400 - 700 nm with a threshold at about 400 nm. The absorption threshold at about 400 nm can be corresponding to the intrinsic band gaps absorption of TiO_2,[75] while the wide absorption in the range of 400 - 700 nm is attributed to the introduction of oxygen vacancies.[76] Its lowering trend suggest the decrease of the oxygen vacancy concentration with the increase of calcination temperature.[76] In addition, electron spin resonance (ESR) was also used to characterize the existence of oxygen vacancies in the prepared TiO_2 samples. Herein, distinctive responses near g value of 2.003 in Figure 2D is related to the typical signals of the unpaired electrons of oxygen vacancies,[77] which shows a decreased trend with the increase of calcination temperature. These results again suggest the decreased oxygen vacancies of OV-C/TiO_2 samples with the increase of calcination temperature, being consistent with the UV-vis DRS results. In brief, fewer oxygen vacancies were formed in the structure of TiO_2 at higher temperatures.

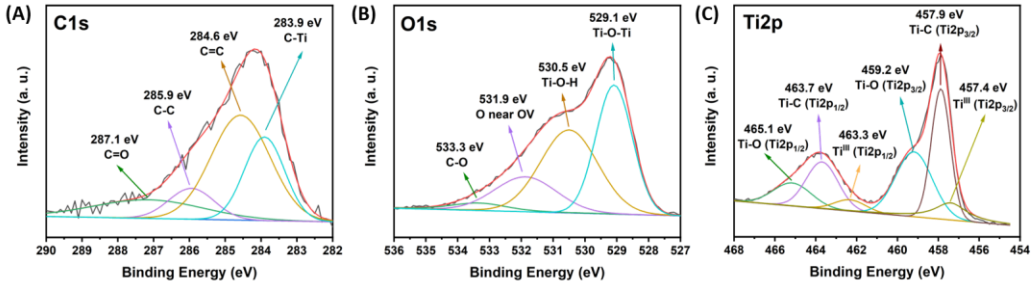

Figure 3 High-resolution XPS spectra of C1s (A), O1s (B) and Ti2p (C) spectra of OV-C/TiO_2-600.

X-ray photoelectron spectroscopy was conducted to investigate the chemical compositions and oxygen vacancies of the prepared OV-C/TiO_2 - 600 sample. The XPS survey spectra in Figure S9 reveal the presence of Ti, O and C in the sample of OV-C/TiO_2-600. Then, the high resolution XPS spectra of C 1s, O 1s and Ti 2p are shown in Figure 3A - C, respectively. The C 1s peak in Figure 3A can be divided into 4 peaks at 287.1 eV, 285.9 eV, 284.6 eV, and 283.9 eV, indicating the carbon of C=O, C-C, C=C and C-Ti species.[45, 52] Four types of oxygen are observed in Figure 3B, and the peaks at 533.3 eV, 531.9 eV, 530.5 eV and 529.1 eV are assigned to adsorption oxygen groups, oxygen near oxygen vacancy, Ti-O-H oxygen and Ti-O-Ti oxygen, respectively.[78] In Figure 3C, two peaks located at 465.1 eV and 459.2 eV are ascribed to Ti $2p_{1/2}$ and Ti $2p_{3/2}$ of typical Ti-O bond in TiO_2, while the peaks at 463.7 eV and 457.9 eV are attributed to Ti-C bond, confirming the doping of carbon in TiO_2.[45] Meanwhile, Ti^{III} vacancy peaks at 463.3 eV and 457.4 eV are also observed, further suggesting the formation of oxygen vacancy.[78] The oxygen vacancies could be formed on the interface between Ti_3C_2 MXene and TiO_2 when C in the crystal of Ti_3C_2 reacted with the closest O in the crystal of TiO_2, releasing CO_2.

Based on the results and discussions, the samples we obtained by Ti_3C_2 MXene oxidation at different temperatures are OV-C/TiO_2 nanoparticles, which can distinctly indicate the structure of the prepared catalyst.

3.2. Photocatalytic fixation of N_2

The prepared OV-C/TiO_2 samples in this work show excellent performances for photocatalytic NH_3 synthesis with both H_2O and CH_3OH as the proton sources. As shown in Figure 4A, all the prepared OV-C/TiO_2 photocatalysts exhibited higher activity for ammonia

production than the commercial anatase-TiO_2 (0 μmol g^{-1} h^{-1}) and P25 (1.55 μmol g^{-1} h^{-1}), when we used H_2O as the proton source. Among them, OV-C/TiO_2-600 generated the most NH_3 with the rate of 41 μmol g^{-1} h^{-1}, although it has 3 times smaller surface area (16.9 m^2 g^{-1}) than the referred P25 TiO_2 (50.0 m^2 g^{-1}). However, it is difficult to detect the production of O_2, the product of hole oxidation with H_2O, which may be due to its over low production. Therefore, we tested the production of ·OH formed by the valence hole oxidation under visible light irradiation, with the coumarin method (Figure S10). Further, we used CH_3OH to replace H_2O as the proton source, the photocatalytic production of NH_3 over all the sample were significantly improved (Figure 4B), and the highest NH_3 production was achieved to 84 μmol g^{-1} h^{-1} at OV-V/TiO_2-600. Meanwhile, the generation of HCHO in this system, which was produced by the oxidation of CH_3OH by the valence hole, was also detected by UV-vis absorbance spectra (Figure S11). In addition, the control experiments by commercial anatase TiO_2 particle were also carried out for a comparison. The results in Figure 4C and D further confirm that OV-C/TiO_2-600 photocatalyst is active for photocatalytic N_2 fixation, and negligible NH_3 was observed in the absence of either full spectrum light or N_2. These results indicate that OV-C/TiO_2 is necessary for catalytic synthesis of NH_3, as well as the light irradiation. The prepared OV-C/TiO_2 samples in this work show a comparable NH_3 production rate compare to the other TiO_2-based photocatalysts over the past 5 years (Table S3). This outstanding N_2 fixation performance of OV-C/TiO_2 reveals the critical role of vacancies introduction. It is worth to note that the concentration of oxygen vacancy and C doping in photocatalysts is very important to their photocatalytic activity. As most of the heteroatom doping, oxygen vacancy and C introduction acts not only as the separation center of photogenerated carriers, but also as the recombination center of photogenerated carriers. Therefore, both too much or over low vacancies can not enhance the photocatalytic activity of photocatalyst. This is the main reason for the highest photocatalytic activity was achieved on OV-C/TiO_2-600. In addition, NH_3 generation yields almost remained steady over four photocatalytic cycling experiments, indicating the good stability of OV-C/TiO_2-600 sample (Figure 4E and F). The apparent quantum yields (AQY) of the photocatalytic N_2 reduction over the prepared OV-C/TiO_2-600 were also measured under the homogeneous light, with H_2O as the proton source. They are 0.04% for the light of 400 nm and 0.01% for the light of 420 nm, respectively (Figure S12).

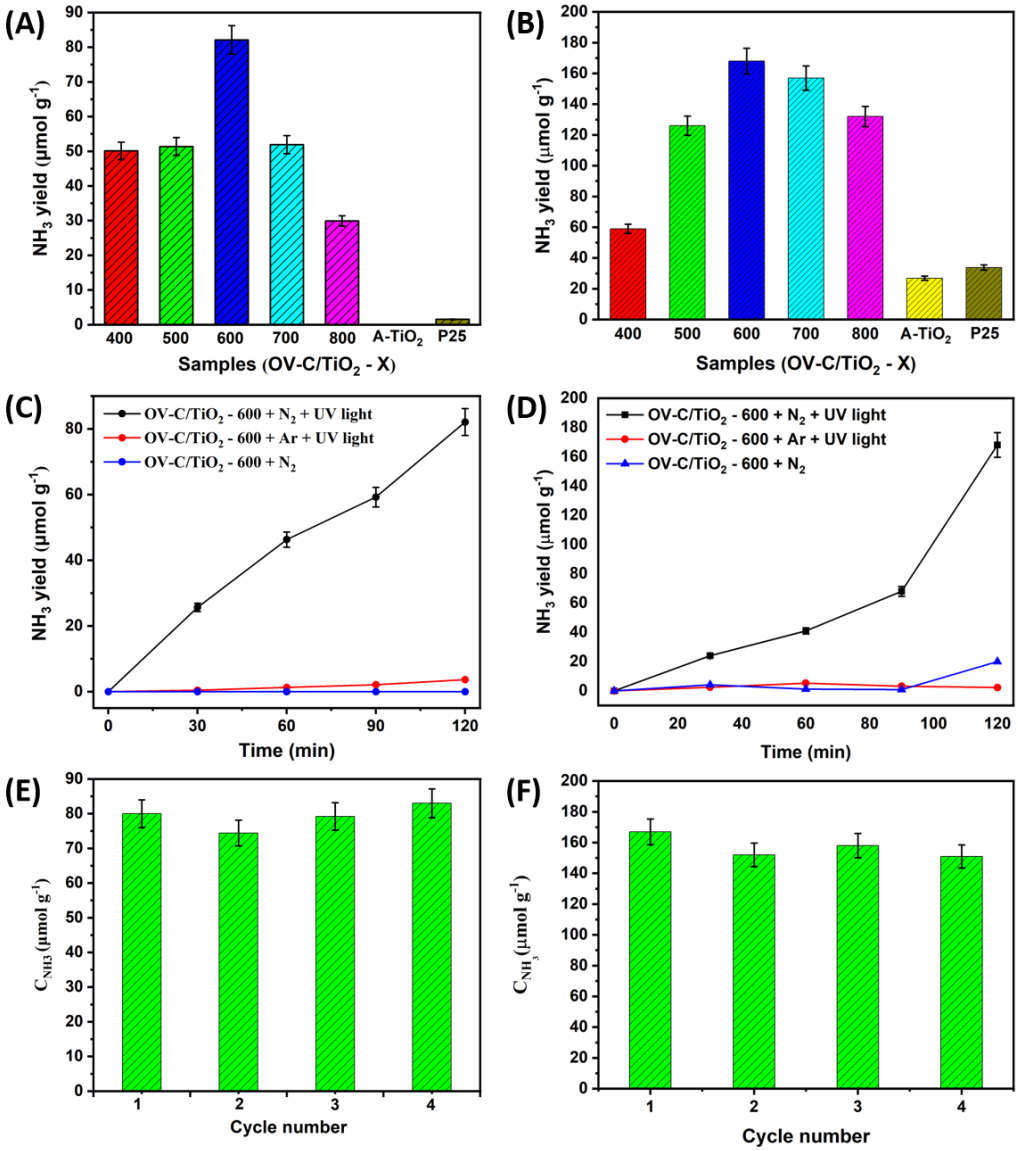

Figure 4 (A) NH_3 generation on OV-C/TiO_2 under UV-vis illumination for 2 hours with H_2O as the proton source, (B) NH_3 generation on OV-C/TiO_2 under UV-vis illumination for 2 hours with CH_3OH as the proton source, (C) Control experiments of NH_3 generations for OV-C/TiO_2-600 with H_2O as the proton source, (D) Control experiments of NH_3 generations for OV-C/TiO_2-600 with CH_3OH as the proton source, (E) Cycling experiments of NH_3 synthesis in 2 hours on OV-C/TiO_2-600, with H_2O as the proton source, (F) Cycling experiments of NH_3 synthesis in 2 hours on OV-C/TiO_2-600, with CH_3OH as the proton source.

Isotope labeling experiments were conducted to confirm that the N source of the produced NH_3. According to the previous report,[58] the experimental results by OV-C/TiO_2-600 using $^{14}N_2$

and $^{15}N_2$ as the feeding gas are clearly shown in Figure 5. Being consisted with the standard data in Figure S1, the isotope labeling experimental results support that the produced NH_3 is generated from the direct photo-reduction of N_2 over OV-C/TiO_2.

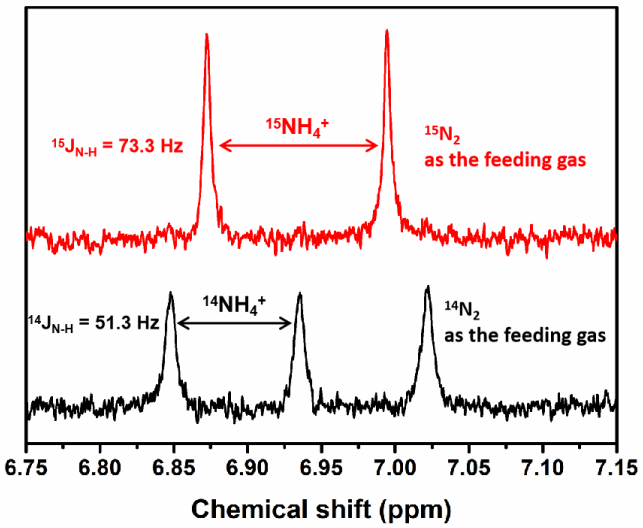

Figure 5 ^{1}H NMR spectra of $^{15}NH_4^+$ and $^{14}NH_4^+$ ions produced by OV-C/TiO_2 using $^{15}N_2$ and $^{14}N_2$ as the feeding gas.

3.3. Mechanism

In order to further understand the underlying mechanism on the high photocatalytic N_2 fixation performance over OV-C/TiO_2-600, some more experiments were carried out. Firstly, photocurrent densities were measured to investigate the generations of electron-hole pairs. As displayed in Figure 6A, the photocurrent density of OV-C/TiO_2-600 is slightly larger than those of other samples, suggesting the highest charge generation rate.[1] Secondly, electrochemical impedance spectra both under the light irradiation (Figure 6B) and in the dark (Figure S13) were also performed to study the charge migration of the prepared OV-C/TiO_2 samples. Smaller diameter of the semi-circle in a Nyquist plot means a smaller charge-transfer resistance for a photocatalyst.[12] The OV-C/TiO_2-600 shows the significantly smallest diameters among all the samples both with and without light irradiation, indicating the smallest charge-transfer resistance. Meanwhile, the charge resistances under light irradiation of all the samples are smaller than those in the dark, which may be caused by the electron excitation. Lastly, the lifetime data of the

photocarriers collected from the time-resolved photoluminescence spectra (Table S4) show that OV-C/TiO_2-600 has the longest average decay time (5.58 ns) compared with other samples (commercial TiO_2: 4.80 ns; OV-C/TiO_2-400: 2.88 ns; OV-C/TiO_2-500: 3.35 ns; OV-C/TiO_2-700: 5.44 ns; OV-C/TiO_2-800: 4.08 ns). Longer decay time implies a longer lifetime of the photogenerated charge carriers. The high generation rate, efficient charge migration and long lifetime of photogenerated electron-hole pairs on OV-C/TiO_2-600 are considered to be the main reasons of the highest photocatalytic activity for N_2 fixation, which was caused by the abundance of oxygen vacancies and carbon doping of the sample. However, oxygen vacancies and doped C can not only act as the separation center, but also work as the recombination center of the photogenerated electron-hole pairs.[23] As the optimized adjustment between these two roles, OV-C/TiO_2-600 shows the biggest photocurrent density and longest decay time.

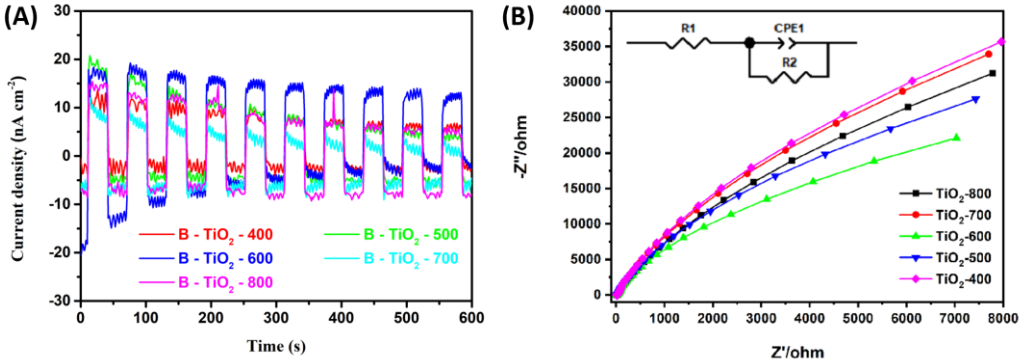

Figure 6 (A) Photocurrent responses of OV-C/TiO_2 derived by Ti_3C_2 MXene calcined at different temperatures, (B) Electrochemical impedance spectra Nyquist plots of OV-C/TiO_2 derived by Ti_3C_2 calcined at different temperatures under full spectrum light illuminations, inset: the equivalent circuit.

The adsorption of N_2 on OV-C/TiO_2-600 was next observed by ESR spectra in Ar and N_2 atmosphere, respectively. As observed in Figure S14, the signal of oxygen vacancies in N_2 atmosphere is much weaker than that in Ar, which attributed to the efficient adsorption of N_2 on oxygen vacancies. Actually, our previous study has also demonstrated that oxygen vacancy is an efficient chemisorption and activation point of N_2 molecular by DFT calculation, with larger combination energy release, longer N≡N bond and shorter N-Ti distances than clean TiO_2 surface.[45] In view of that the chemisorption is an essential step during the photocatalytic N_2

reduction processes, N_2-temperature-programmed desorption (N_2-TPD) was further performed to peruse the adsorption-desorption activation of N_2 on the surface of the prepared OV-C/TiO_2. Referencing the previous report,[79] the chemisorption of N_2 usually occurs at about 280 ℃ (on carbon) and 360 ℃ (on TiO_2), while the physical adsorption of N_2 occurs at about 120 ℃. As displayed in Figure 7, the remarkable higher TCD signal of OV-C/TiO_2 than that of the commercial anatase TiO_2 shows the much better chemisoption of N_2 on the surface of OV-C/TiO_2 than that of the commercial anatase, which is crucial for the N_2 activation.

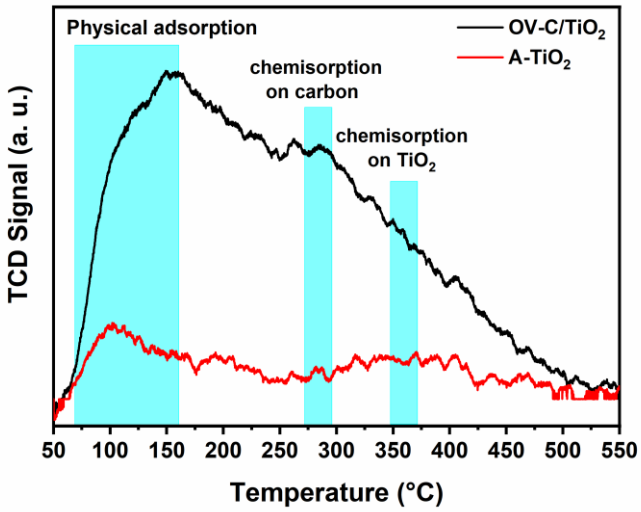

Figure 7 N_2-TPD profiles of the commercial anatase TiO_2 and OV-C/TiO_2-600.

Following with the adsorption of N_2 (step ①), there are 6 steps of hydrogenation and 2 steps of NH_3 desorption, as described in Figure 8. In this work, we further calculate the free energy and bond changes of N-N & N-Ti of every step, to describe the reaction pathways of N_2 conversion to NH_3 on the oxygen vacancy on TiO_2 surface. The optimized structures of selected N_2 reduction reaction intermediates are presented in Figure S15-23. As shown in Figure 8, N_2 on the oxygen vacancy on TiO_2 surface is reduced through an "alternating" pathway, being started from "distal" and finished by "enzymatic" pathways.[80] The two N atoms in the N_2 molecules become asymmetric when it is adsorbed on the oxygen vacancy, resulting in the polarization of N≡N bond. Table S5 lists the bond distance changes of N-N and N-Ti with the hydrogenation and NH_3 desorption steps, listing the activation process of N_2 conversion to NH_3 on the oxygen site on TiO_2 surface. Detailedly, the hydrogenation steps are exothermic processes (③: -0.68 eV; ④: -0.16 eV, ⑤: -0.13 eV and ⑥:

-2.66 eV) except step ② to form *N=NH from *N_2 (+0.06 eV) and step ⑧ to form *NH_2 from *NH_3 (+0.37 eV), while the NH_3 desorption steps are endothermic processes (⑦: +0.06 eV and ⑨: +0.69 eV). Based on these results, the reaction of N_2 in the oxygen vacancy on TiO_2 surface reduction to NH_3 is dominated by a Gibbs free energy releasing process, and the potential determining step (PDS) is ascertained to be the last step involved in the second NH_3 desorption, which is consisted with the experimental results that the generated NH_3 can absolutely desorb into the solution only after reacting with 0.1M HCl regent. Our DFT calculations demonstrated that oxygen vacancy can effectively polarize N≡N bond and reduce it through a Gibbs free energy release leading alternating pathway with the second NH_3 desorption as the PDS.

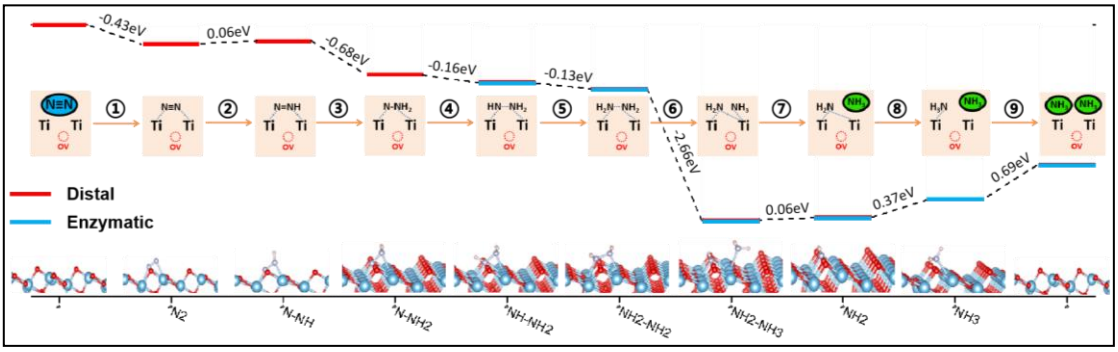

Figure 8 Minimum energy path for the N_2 conversion into NH_3 in the site of oxygen on the surface of TiO_2.

Overall, based on the studies and discussions above, a schematic illustration of photocatalytic N_2 fixation over OV-C/TiO_2 with oxygen vacancies is displayed in Scheme 2. With the doping of oxygen vacancy and carbon in the crystal of TiO_2, defect energy levels were introduced in the middle of forbidden zone, forming heteroatom energy band above the valence band[81] and vacancy energy band[12] under the conduction band. The specific band structure of OV-TiO_2-600 was obtained by the Tauc-plot curve (Figure S24) and Mott-schokkty plots (Figure S25). Upon the irradiation of full spectrum light, electrons on the valence band of TiO_2 are excited and populated into the conduction band or vacancy states. Then the excited electrons on both the conduction band and defect states react with N_2 adsorbed on oxygen vacancies, producing NH_3 molecular. Meanwhile, the holes will react with CH_3OH. Several reasons can explain the enhanced N_2 fixation activity. Firstly, oxygen vacancies and doping carbon can broaden the range of the light absorbance, which helps to provide more electron-hole pairs and promote their separations;

secondly, oxygen vacancies capture the electrons on the conduction band, resulting in a prolonged lifetime of photocarriers; thirdly, oxygen vacancies act as adsorption and activation sites for N_2 , enhancing and increasing the N_2 conversion to NH_3 through a Gibbs free energy decrease leading alternating pathway with a low energy barriers.

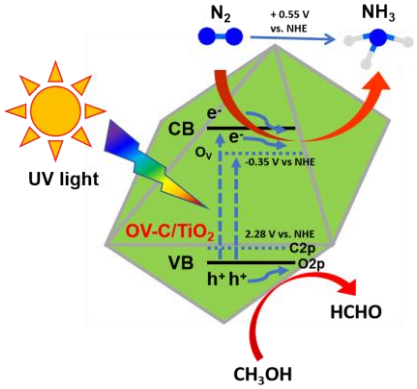

Scheme 2 Diagram of the photocatalytic N_2 fixation mechanism over OV-C/TiO_2.

4. Summary

In summary, OV-C/TiO_2 with the abundance of oxygen vacancies were successfully prepared by calcining Ti_3C_2 MXene at different temperatures. Notably, this strategy can control the amount of oxygen vacancy through a facial and reproducible process. All the prepared OV-C/TiO_2 catalysts show excellent photocatalytic N_2 fixation performance, which achieved the highest of 84 μmol g^{-1} h^{-1} at OV-C/TiO_2 with CH_3OH as the proton source, much higher than P25 and commercial A-TiO_2. The introductions of oxygen vacancies and carbon doping are the most crucial factor for such significant photocatalytic N_2 fixation performance, which not only enhance the generation of electron-hole pairs, reduce the recombination of electron-hole pairs, but also prolong the lifetime of photocarriers and enhance the chemisorption & activation of N_2 molecular. Most importantly, oxygen vacancies play efficient N_2 absorption site and active the N_2 atoms trough a Gibbs free energy releasing leading pathway. The efficiency of photocatalytic N_2 fixation by TiO_2 is thus lifted to a high level, although it is still too low to realize the practical applications.

Acknowledgments

J. Q., S. Z., Y. L., W. Z., L. L., and H.-Y. J. are grateful for the financial supports of this work from

Supported by National Natural Science Foundation of China (No. 21703170), Key Research and Development Program of Shaanxi (No. 2020GY-244), Yong Academic Talents Program of Northwest University and Top-rated Discipline construction scheme of Shaanxi higher education. J. W. T. and H. W. are thankful for financial support from UK EPSRC (EP/N009533/1), Royal Society-Newton Advanced Fellowship grant (NA170422) and the Leverhulme Trust (RPG-2017-122). W. D. and H.-Y. J. acknowledge the Innovation Fund Project of Colleges and Universities of Gansu Province (No. 2020A-097).

References

1. H. Li, J. Shang, Z. Ai, L. Zhang, *J. Am. Chem. Soc.* **2015**, *132*, 6393-6399.
2. L. Li, Y. Wang, S. Vanka, X. Mu, Z. Mi, C.-J. Li, *Angew. Chem.* **2017**, *129*, 8827-8831.
3. D. Zhu, L. Zhang, R. E. Ruther, R. J. Hamers, *Nat. Mater.* **2013**, *12*, 836-841.
4. H. Hirakawa, M. Hashimoto, Y. Shiraishi, T. Hirai, *J. Am. Chem. Soc.* **2017**, *139*, 10929-10936.
5. A. Banerjee, B. D. Yuhas, E. A. Margulies, Y. Zhang, Y. Shim, M. R. Wasielewski, M. G. Kanatzidis, *J. Am. Chem. Soc.* **2015**, *137*, 2030-2034.
6. K. A. Brown, D. F. Harris, M. B. Wilker, A. Rasmussen, N. Khadka, H. Hamby, S. Keable, G. Dukovic, J. W. Peters, L. C. Seefeldt, P. W. King, *Science* **2016**, *352*, 448-450.
7. T. Rayment, R. Schlogl, J. M. Thomas, G. Ertl, *Nature* **1985**, *315*, 311-313.
8. D. E. Canfield, A. N. Clazer, P. G. Falkowski, *Science* **2010**, *330*, 192-196.
9. C. J. M. van der Ham, M. T. M. Koper, D. G. H. Hetterscheid, *Chem. Soc. Rev.* **2014**, *43*, 5183-5191.
10. C. Guo, J. Ran, A. Vasileff, S.-Z. Qiao, *Energy Environ. Sci.* **2018**, *11*, 45-56.
11. G. Marnellos, M. Stoukides, *Science* **1998**, *282*, 98-100.

12. Y. Zhao, Y. Zhao, R. Shi, B. Wang, G. I. M. Waterhouse, L.-Z. Wu, C.-H. Tung, T. Zhang, *Adv. Mater.* **2019**, *31*, 1806482.

13. T. Oshikiri, K. Ueno, H. Misawa, *Angew, Chem.* **2016**, *128*, 4010-4014.

14. X. Chen, N. Li, Z. Kong, W.-J. Ong, X. Zhao, *Mater. Horiz.* **2018**, *5*, 9-27.

15. G. N. Schrauzer, T. D. Guth, *J. Am. Chem. Soc.* **1977**, *99*, 7189-7193.

16. W. Zhao, B, Liu, J. Qin, J. Ke, L. Yu, X. Xu, *ChemPhotoChem.* **2020**, doi: 10.1002/cptc.202000114.

17. S.-F. Ng, M. Y. L. Lau, W.-J. Ong, *Solar RRL* **2020**, doi: 10.1002/solr.202000535.

18. S. Chen, D. Liu, T. Peng, *Solar RRL* **2020**, doi: 10.1002/solr.202000487.

19. L. Shi, Y. Yin, S. Wang, H. Sun, *ACS Catal.* **2020**, *10*, 6870-6899.

20. Z. Wang, J. Hong, S.-F. Ng, W. Liu, J. Huang, P. Chen, W.-J. Ong, *Acta Phys.-Chim. Sin.* **2021**, *37*, 2011033

21. X. Xue, R. Chen, C. Yan, P. Zhao, Y. Hu, W. Zhang, S. Yang, Z. Jin, *Nano Res.* **2019**, *12*, 1229-1249.

22. W.-J. Ong, K. P. Y. Shak, *Solar RRL*, **2020**, *4*, 2000132.

23. S. Wang, X. Hai, X. Ding, K. Chang, Y. Xiang, X. Meng, Z. Yang, H. Chen, J. Ye, *Adv. Mater.* **2017**, *29*, 1701774.

24. C. Li, T. Wang, Z.-J. Zhao, W. Yang, J.-F. Li, A. Li, Z. Yang, G. A. Ozin, J. Gong, *Angew. Chem. Int. Ed.* **2018**, *57*, 5278-5282.

25. S. Bourgeous, D. Diakite, M. Perdereau, *React. Solids* **1988**, *6*, 95-104.

26. J. Soria, J. Conesa, V. Auguliaro, L. Palmisano, M. Schiavello, A. Sclafani, *J. Phys. Chem.* **1991**, *95*, 274-282.

27. W. Zhao, J. Zhang, X. Zhu, M. Zhang, J. Tang, M. Tan, Y. Wang, *Appl. Catal. B: Environ.* **2014**, *144*, 468-477.

28. L. Palmisano, V. Augugliaro, A. Sclafani, M. Schiavello, *J. Phys. Chem.* **1988**, *92*, 6710-6713.

29. O. Ileperuma, K. Tennakone, W. Dissanayake, *Appl. Catal.* **1990**, *62*, L1-L5.

30. O. Ileperuma, C. Thaminimulla, W. Kiridena, *Sol. Energy Mater. Sol. Cells* **1993**, *28*, 335-343.

31. K. T. Ranjit, T. K. Varadarajan, B. Viswanathan, *J. Photochem. Photobiol.* **1996**, *96*, 181-185.

32. K. Hoshino, *Chem. Eur. J.* **2001**, *7*, 2727-2731.

33. T. Oshikiri, K. Ueno, H. Misawa, *Angew. Chem. Int. Ed.* **2014**, *53*, 9802-9805.

34. Q.-S. Li, K. Domen, S. Naito, T. Onishi, K. Tamaru, *Chem. Lett.* **1983**, *12*, 321-324.

35. H. Li, J. Shang, J. Shi, K. Zhao, L. Zhang, *Nanoscale* **2016**, *8*, 1986-1993.

36. Y. Bai, L. Ye, T. Chen, L. Wang, X. Shi, X. Zhang, D. Chen, *ACS Appl. Mater. Interfaces* **2016**, *8*, 27661-27668.

37. Y. Wang, W. Wei, M. Li, S. Hu, J. Zhang, R. Feng, *RSC Adv.* **2017**, *7*, 18099-18107.

38. G. Dong, W. Ho, C. Wang, *J. Mater. Chem. A* **2015**, *3*, 23435-23441.

39. S. Hu, Y. Li, F. Li, Z. Fan, H. Ma, W. Li, X. Kang, *ACS Sustainable Chem. Eng.* **2016**, *4*, 2269-2278.

40. Q. Zhang, S. Hu, Z. Fan, D. Liu, Y. Zhao, H. Ma, F. Li, *Dalton Trans.* **2016**, *45*, 3497-3505.

41. S. Hu, W. Zhang, J. Bai, G. Lu, L. Zhang, G. Wu, *RSC Adv.* **2016**, *6*, 25695-25702.

42. H. Liang, H. Zou, S. Hu, *New J. Chem.* **2017**, *41*, 8920-8926.

43. Y. Liu, M. Cheng, Z. He, B. Gu, C. Xiao, T. Zhou, Z. Guo, J. Liu, H. He, B. Ye, B. Pan, Y. Xie, *Angew. Chem. Int. Ed.* **2019**, *58*, 731-735.

44. M. Naguib, M. Kurtoglu, V. Presser, J. Lu, J. Niu, M. Heon, L. Hultman, Y. Gogotsi, M. W. Barsoum, *Adv. Mater.* **2011**, *23*, 4248-4253.

45. Y. Liao, J. Qian, G. Xie, Q. Han, W. Dang, S. Wang, L. Lv, S. Zhao, L. Luo, W. Zhang, H.-Y.

Jiang, J. Tang, *Appl. Catal. B: Environ.* **2020**, *273*, 119054.

46. T. Cai, L. Wang, Y. Liu, S. Zhang, W. Dong, H. Chen, X. Yi, J. Yuan, X. Xia, C. Liu, S. Lou, *Appl. Catal. B: Environ.* **2018**, *239*, 545-554.

47. J. Ran, G. Gao, F.-T. Li, T.-Y. Ma, A. Du, S.-Z. Qiao, *Nat. Commun.* **2017**, *8*, 13907.

48. S. Cao, B. Shen, T. Tong, J. Fu, J. Yu, *Adv. Func. Mater.* **2018**, *28*, 1800136.

49. Z. Zeng, Y. Yan, J. Chen, P. Zan, Q. Tian, P. Chen, *Adv. Func. Mater.* **2019**, *29*, 1806500.

50. L. Cheng, Q. Chen, J. Li, H. Liu, *Appl. Catal. B: Environ.* **2020**, *267*, 118379.

51. Y. Sun, D. Jin, Y. Sun, X. Meng, Y. Gao, Y. Dall'Agnese, G. Chen, X.-F. Wang, *J. Mater. Chem. A* **2018**, *6*, 9124-9131.

52. W. Yuan, L. Cheng, Y. Zhang, H. Wu, S. Lv, L. Chai, X. Guo, L. Zheng, *Adv. Mater. Interfaces* **2017**, *4*, 1700577.

53. W. Yuan, L. Cheng, Y. An, S. Lv, H. Wu, X. Fan, Y. Zhang, X. Guo, J. Tang, *Adv. Sci.* **2018**, *4*, 1700870.

54. Y. Fang, Z. Liu, J. Han, Z. Jin, Y. Han, F. Wang, Y. Niu, Y. Wu, Y. Xu, *Adv. Energy Mater.* **2019**, *9*, 1803406.

55. Y. Zhao, R. Shi, X. Bian, C. Zhou, Y. Zhao, S. Zhang, F. Wu, G. I. N. Waterhouse, L.-Z. Wu, C.-H. Tung, T. Zhang, *Adv. Sci.* **2019**, *6*, 1802109.

56. H.-Y. Jiang, G. Liu, M. Li, J. Liu, W. Sun, J. Ye, J. Lin, *Appl. Catal. B: Environ.* **2015**, *163*, 267-276.

57. H. Song, X. Meng, S. Wang, W. Zhou, X. Wang, T. Kako, J. Ye, *J. Am. Chem. Soc.* **2019**, *141*, 20507-20515.

58. L. Zhang, L.-X. Ding, G.-F. Chen, X. Yang, H. Wang, *Angew. Chem. Int. Ed.* **2019**, *58*, 2612-2616.

59. P. E. Blöchl, *Phys. Rev. B* **1994**, *50*, 17953.

60. G. Kresse, D. Joubert, *Phys. Rev. B* **1999**, *59*, 1758.

61. G. Kresse, J. Furthmüller, *Phys. Rev. B* **1996**, *54*, 11169.

62. J. P. Perdew, K. Burke, M. Ernzerhof, *Phys. Rev. Lett.* **1996**, *77*, 3865.

63. H. J. Monkhorst, J. D. Pack, *Phys. Rev. B* **1976**, *13*, 5188.

64. S. Grimme, *J. Comput. Chem.* **2006**, *27*, 1787.

65. S. Grimme, J. Antony, S. Ehrlich, S. Krieg, *J. Chem. Phys.* **2010**, *132*, 154104.

66. S. Grimme, S. Ehrlich, L. Georigk, *J. Comp. Chem.* **2011**, *32*, 1456.

67. K. Momma, F. Izumi, *J. Appl. Crystallogr.* **2011**, *44*, 1272.

68. Y. Zhao, C. Chang, F. Teng, Y. Zhao, G. Chen, R. Shi, G. I. N. Waterhouse, W. Huang, T. Zhang, *Adv. Energy Mater.* **2017**, *7*, 1700005.

69. Y. Ping, R. J. Nielsen, W. A. Goddard, *J. Am. Chem. Soc.* **2017**, *139*, 149.

70. H. Li, J. Shang, J. Shi, K. Zhao, L. Zhang, *Nanoscale* **2016**, *8*, 1986.

71. M. Kruk, M. Jaroniec, *Chem. Mater.* **2001**, *13*, 3169-3183.

72. X. An, Q. Tang, H. Lan, H. Liu, J. Qu, *Appl. Catal. B: Environ.* **2019**, *244*, 407-413.

73. H.-Y. Jiang, J. Liu, K. Cheng, W. Sun, J. Lin, *J. Phys. Chem. C* **2013**, *117*, 20029-20036.

74. S. Chen, Y. Xiao, Y. Wang, Z. Hu, H. Zhao, W. Xie, *Nanomater.* **2018**, *8*, 245.

75. K. Cheng, W. Sun, H.-Y. Jiang, J. Liu, J. Lin, *J. Phys. Chem. C* **2013**, *117*, 14600-14607.

76. H. Song, C. Li, Z. Lou, Z. Ye, L. Zhu, *ACS Sustainable Chem. Eng.* **2017**, *5*, 8982-8987.

77. J. Wan, W. Chen, C. Jia, L. Zheng, J. Dong, X. Zheng, Y. Wang, W. Yan, C. Chen, Q. Peng, D. Wang, Y. Li, *Adv. Mater.* **2018**, *30*, 1705369.

78. X. Kong, Y. Xu, Z. Cui, Z. Li, Y. Liang, Z. Gao, S. Zhu, X. Yang, *Appl. Catal. B: Environ.* **2018**, *230*, 11-17.

79. Q. Liu, L. Ai, J. Jiang, *J. Mater. Chem. A* **2018**, *6*, 4102-4110.

80. M. Shao, Y. Shao, W. Chen, K. L. Ao, R. Tong, Q. Zhu, I. N. Chan, W. F. Ip, X. Shi, H. Pan, *Phys. Chem. Chem. Phys.* **2018**, *20*, 14504.

81. C. Yang, J. Qin, Z. Xue, M. Ma, X. Zhang, R. Liu, *Nano Energy* **2017**, *41*, 1-9.